



Direct growth of single-metal-atom chains

Shasha Guo^{1,15}, Jiecai Fu^{2,3,15}, Peikun Zhang^{4,15}, Chao Zhu^{1,5,15}, Heming Yao⁶, Manzhang Xu¹, Boxing An⁷, Xingli Wang^{1,8}, Bijun Tang¹, Ya Deng¹, Teddy Salim¹, Hongchu Du^{1,2,9}, Rafal E. Dunin-Borkowski², Mingquan Xu¹⁰, Wu Zhou¹⁰, Beng Kang Tay^{8,11}, Chao Zhu¹, Yanchao He¹, Mario Hofmann¹², Ya-Ping Hsieh¹³, Wanlin Guo⁴, Michael Ng^{1,6}, Chunlin Jia^{1,2,14}, Zhuhua Zhang^{1,4}, Yongmin He^{1,14} and Zheng Liu^{1,8,11}

Single-metal-atom chains (SMACs), as the smallest one-dimensional structure, have intriguing physical and chemical properties. Although several SMACs have been realized so far, their controllable fabrication remains challenging due to the need to arrange single atoms in an atomically precise manner. Here we develop a chemical vapour co-deposition method to construct a wafer-scale network of platinum SMACs in atom-thin films. The obtained atomic chains possess an average length of up to ~17 nm and a high density of over 10 wt%. Interestingly, as a consequence of the electronic delocalization of platinum atoms along the chain, this atomically coherent one-dimensional channel delivers a metallic behaviour, as revealed by electronic measurements, first-principles calculations and complex network modelling. Our strategy is potentially extendable to other transition metals such as cobalt, enriching the toolbox for manufacturing SMACs and paving the way for the fundamental study of one-dimensional systems and the development of devices comprising monoatomic chains.

Single-metal-atom chains (SMACs), known as the smallest one-dimensional structures, have garnered broad research interest attributing to their unique properties such as quantized conductance, thermal transport, charge/spin density waves and peculiar magnetic properties, as well as distinct catalytic properties^{1–6}. For example, it was reported that the average bond strength in the chain is twice that of the bulk counterpart⁷. Up until now, several SMACs such as gold, iridium and platinum chains have been fabricated by using a top-down mechanical break junction method, exhibiting quantum ballistic transport^{8,9}, anisotropic magnetoresistance^{10,11} and the Kondo effect¹². Alternatively, an ultra-high vacuum self-assembly approach on the ultra-clean substrate was developed for preparing gold SMACs on germanium stepped surfaces^{13–15} and silicon, serving as a one-dimensional model system to study Peierls instabilities and Tomonaga–Luttinger liquid. Unfortunately, these methods require harsh growth conditions. Besides, the mechanical break junction prepared SMACs suffer from short length (<5 atoms in length) and structural fragility, and self-assembled atom wires are extremely unstable under the atmosphere. These characteristics greatly restrict the broad applicability of resultant SMACs, particularly in devices¹⁶; thus, exploring a simple and efficient strategy for the scalable synthesis of SMACs with ambient atmosphere stability is still highly demanded so far.

Inspired by the formation mechanism of the one-dimensional grain-boundary channel in two-dimensional materials^{17–20}, here we report the fabrication of platinum SMACs network within the transition-metal dichalcogenide material film at a wafer scale (5 cm). The mirror twin grain boundary (MTB) acts as an ideal one-dimensional host for platinum atoms, and the obtained platinum SMACs possess an average length of up to 17 nm and remarkable ambient air stability. We further demonstrate that these platinum SMACs are highly metallic, forming a network conduction pathway in the two-dimensional film to enrich their electronic properties and functionalities. Moreover, we have also embedded cobalt SMACs into MTBs of the MoS₂ film, suggesting the generalizability of our strategy for wafer-scale production of ambient air-stable SMACs.

Results and discussion

Synthesis and characterization of platinum SMACs. A chemical vapour co-deposition method was developed to fabricate a platinum SMACs network in a wafer-scale atomically thin MoS₂ film (Fig. 1a) (see Methods for details). Ultra-small platinum nanoclusters (0.5–2 nm) were pre-deposited onto a SiO₂/Si substrate through electron-beam evaporation, followed by the growth of MoS₂. This pre-deposited platinum layer plays two crucial roles in forming platinum SMACs: first, by supplying platinum and, second, serving as

¹School of Materials Science and Engineering, Nanyang Technological University, Singapore, Singapore. ²Ernst Ruska-Centre for Microscopy and Spectroscopy with Electrons and Peter Grünberg Institute, Forschungszentrum Jülich GmbH, Jülich, Germany. ³Key Laboratory for Magnetism and Magnetic Materials of the Ministry of Education, School of Physical Science and Technology, Lanzhou University, Lanzhou, China. ⁴State Key Laboratory of Mechanics and Control of Mechanical Structures, Key Laboratory for Intelligent Nano Materials and Devices of Ministry of Education, and Institute for Frontier Science, Nanjing University of Aeronautics and Astronautics, Nanjing, China. ⁵SEU-FEI Nano-Pico Center, Key Lab of MEMS of Ministry of Education, School of Electronic Science and Engineering, Southeast University, Nanjing, China. ⁶Department of Mathematics, The University of Hong Kong, Hong Kong, China. ⁷College of Materials Science and Engineering, Beijing University of Technology, Beijing, China. ⁸CINTRA CNRS/NTU/THALES, UMI 3288, Research Techno Plaza, Singapore, Singapore. ⁹Central Facility for Electron Microscopy, RWTH Aachen University, Aachen, Germany. ¹⁰School of Physical Sciences, CAS Key Laboratory of Vacuum Physics, University of the Chinese Academy of Sciences, Beijing, China. ¹¹School of Electrical and Electronic Engineering, Nanyang Technological University, Singapore, Singapore. ¹²Department of Physics, National Taiwan University, Taipei, Taiwan. ¹³Institute for Atomic and Molecular Sciences, Academia Sinica, Taipei, Taiwan. ¹⁴State Key Laboratory of Chemo/Biosensing and Chemometrics, College of Chemistry and Chemical Engineering, Hunan University, Changsha, China. ¹⁵These authors contributed equally: Shasha Guo, Jiecai Fu, Peikun Zhang, Chao Zhu. ✉e-mail: c.jia@fz-juelich.de; chuwazhang@nuaa.edu.cn; ymhe@hnu.edu.cn; z.liu@ntu.edu.sg

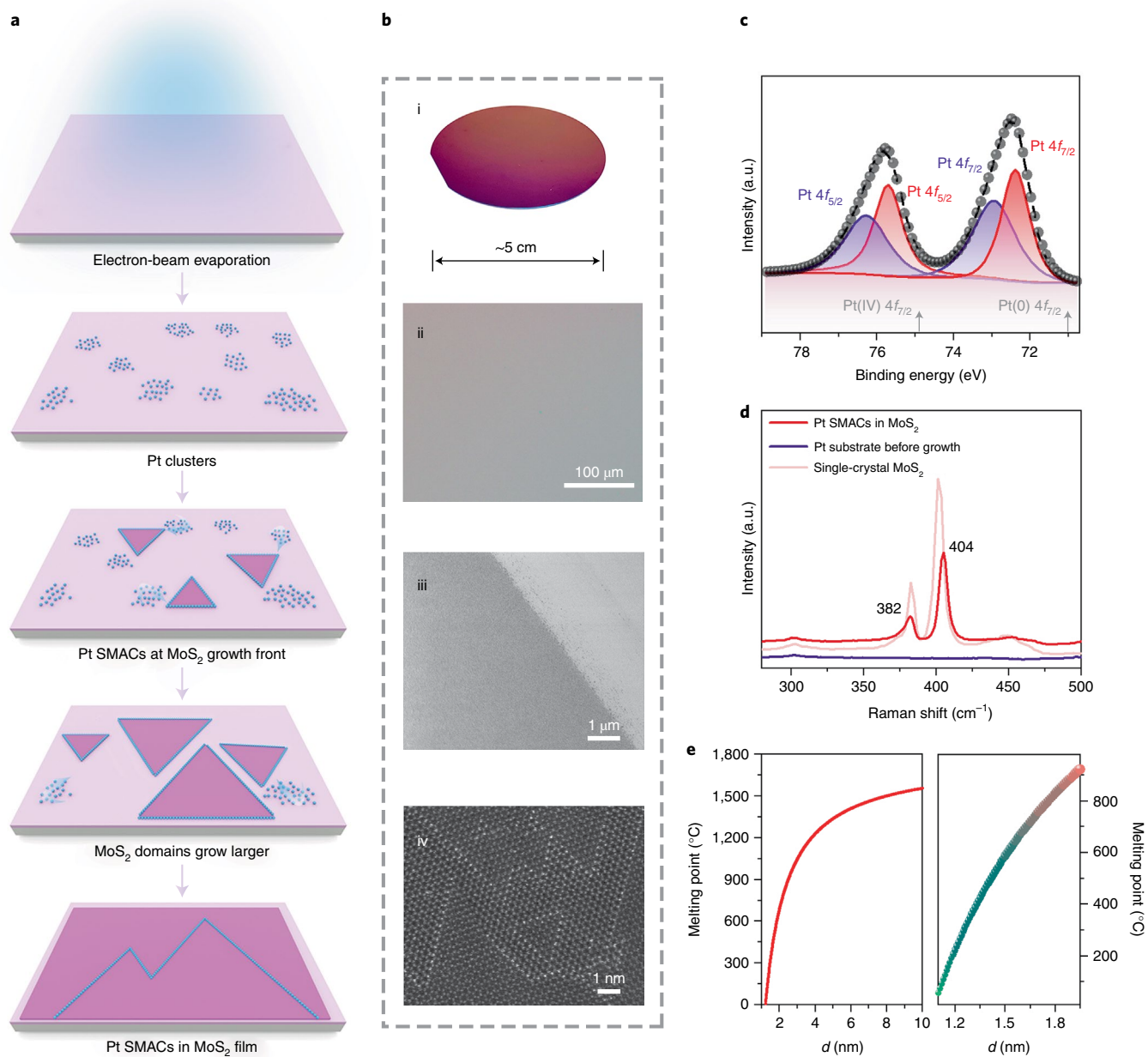


Fig. 1 | Growth of platinum SMACs. **a**, Schematic of the fabrication process with two typical steps: first, high-density platinum atom-clusters were deposited onto a SiO_2/Si substrate by electron-beam evaporation at a rate of 0.1 \AA s^{-1} ; second, platinum SMACs were formed during the growth of MoS_2 films. **b**, Platinum SMACs/ MoS_2 film from wafer-scale to nanoscale, including a photograph (i), optical image (ii), SEM image (iii) and an atomically resolved ADF-STEM image (iv). The bright dotted lines in iv show the contrast of platinum SMACs. No massive platinum particle is observed in the MoS_2 nanograin film. **c**, Platinum $4f$ XPS spectrum of as-grown film, in which two pairs of peaks were deconvoluted at 72.38, 75.71, 72.94 and 76.28 eV, which are attributed to the first type of Pt(II) $4f_{7/2}$, the first type of Pt(II) $4f_{5/2}$, the second type of Pt(II) $4f_{7/2}$ and the second type of Pt(II) $4f_{5/2}$, respectively. Grey arrows mark the location of Pt(0) and Pt(IV). The scatter plot results from fitting the raw data (dashed black line). **d**, Raman spectra of samples before and after MoS_2 nanograin film growth, and CVD-grown single-crystal MoS_2 . **e**, Left: the relationship between the melting point and the diameter for platinum nanoparticles; right, a magnified illustration of melting states for clusters with diameter $\leq 2 \text{ nm}$ at $650 \text{ }^\circ\text{C}$ (melted drops in blue and unmelted clusters in red). The clusters with a diameter smaller than 1.56 nm will melt at $650 \text{ }^\circ\text{C}$.

nucleation sites to induce the formation of a grain-boundary-rich MoS_2 film (Fig. 1b). Highly dense platinum nanoclusters with an average spacing of down to a few nanometres can be obtained by using low-rate evaporation (0.1 \AA s^{-1}) in our experiment (Supplementary Figs. 1 and 2). It enables the growth of high-density MoS_2 nanograins that provide abundant one-dimensional channels for platinum atom incorporation (Supplementary Fig. 8). As shown in Fig. 1e, these ultra-small platinum nanoclusters tend to become a liquid phase at

the growth temperature of MoS_2 ($600\text{--}750 \text{ }^\circ\text{C}$)²¹. Such liquid nanodroplets facilitate the diffusion of platinum atoms, which are further captured by MoS_2 domains to form thermodynamically stable structures. In short, platinum nanoclusters drive the growth of the grain-boundary-rich MoS_2 film. These dense grain boundaries provide anchor sites for mobile platinum atoms, yielding single-atom-chain structures. Figure 1b presents macroscopic to atomic views of as-grown platinum SMACs in a wafer-scale MoS_2 film.

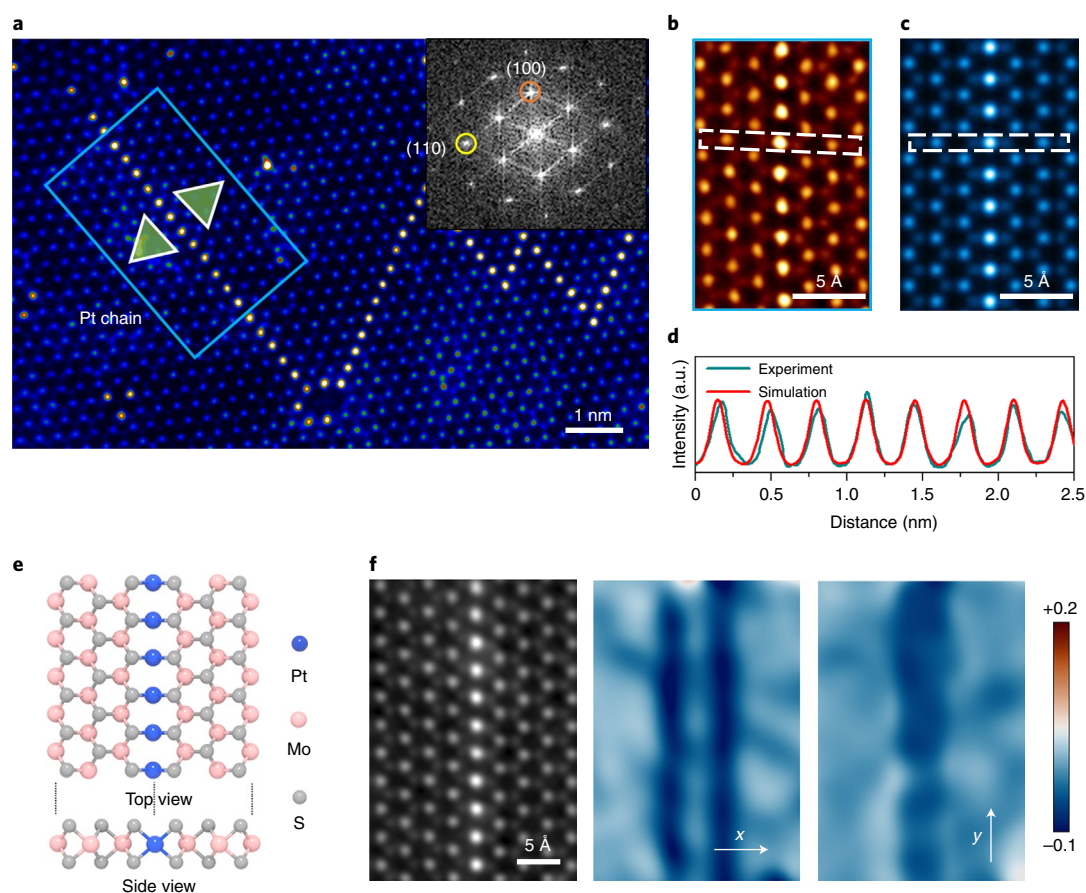


Fig. 2 | Atomic structure of platinum SMACs in monolayer MoS₂. **a**, False-coloured ADF-STEM image of platinum SMACs in monolayer MoS₂. Inset: a fast Fourier transformation of the blue rectangular area. **b**, Magnified ADF-STEM image of a single platinum chain obtained from the blue rectangular area in **a**. **c**, Simulated ADF-STEM imaging of a platinum chain. The intensity profiles along the white dashed boxes in **b-c** are shown in Supplementary Fig. 10. **d**, Intensity profiles of the experimental and simulated images along the platinum SMACs in **b-c**. The average interatomic distance in the chain is measured as 3.2 Å. **e**, Schematic of the detailed atomic structure of the platinum SMAC in monolayer MoS₂. **f**, Magnified ADF-STEM image of a platinum SMAC in monolayer MoS₂ (left), and strain mapping with uniaxial strain components ϵ_{xx} (middle) and ϵ_{yy} (right), as obtained by GPA of the ADF-STEM image.

We next used X-ray photoelectron spectroscopy (XPS) and Raman spectroscopy to investigate the bonding states and the detailed structure of platinum SMACs. As shown in Fig. 1c, two sets of Pt(II) peaks can be clearly observed in the platinum 4f region, which correspond to two kinds of Pt(II) in different chemical environments. The absence of metallic platinum peaks indicates that all platinum atoms are covalently bonded with sulfur atoms instead of being physically adsorbed onto the MoS₂ surface or isolated as particles. Furthermore, large-area XPS analysis reveals an average platinum mass loading as high as ~13 wt%, implying a high density of SMACs achieved by this method. Notably, the mass loading achieved in our work is much higher than that of atomically dispersed platinum atoms (~5 wt%) in other works. Figure 1d presents the Raman spectra of as-grown films. Given that the in-plane to out-of-plane mode ratio is a widely adopted metric to evaluate the crystallinity of MoS₂, our sample has a much smaller intensity ratio (0.28) than currently reported chemical vapour deposition (CVD)-grown (~1.89) and physically exfoliated (~1.57) samples (Supplementary Table 1), suggesting a polycrystalline nature with high-density grain boundaries. After examining tens of regions, we hardly observe peaks associated with PtS₂ or PtS, thus confirming that most platinum atoms are covalently bonded with sulfur atoms at the MoS₂ MTB instead of forming PtS₂ or PtS particles, which is also in agreement with the above XPS results.

We then examined the atomic structure of platinum SMACs in the monolayer MoS₂ film using annular dark-field scanning

transmission electron microscopy (ADF-STEM) imaging, wherein platinum atoms with a high Z-contrast could be clearly identified (Fig. 2a). The corresponding fast Fourier transformation pattern (viewed from the zone axis of <001> in the inset of Fig. 2a) presents a diffraction spot configuration of hexagonal arrangement, confirming the formation of 60° rotation inversion domains. It can be seen that the majority of platinum atoms reside exactly at the MTB to form a single chain. In addition, a small amount of dispersed platinum atoms are also observed in our sample, which is due to the filling of platinum atoms in native vacancies inevitably introduced during the CVD process^{22,23} to minimize the system energy. We examined the blue rectangular region highlighted in Fig. 2a to probe the local environment surrounding the platinum atoms. It turns out that platinum atoms form an atomically coherent one-dimensional channel at the twin boundary (60°) (Fig. 2b), which agrees well with the simulated results in Fig. 2c. The corresponding intensity profiles along platinum SMACs indicate that the distance between adjacent platinum atoms is around 3.2 Å (Fig. 2d), much larger than the conventional Pt-Pt bonds, that is, 2.78 Å in the (111) plane^{24,25}. The above observations suggest a unique structure of our highly ordered platinum single-atom-chain (see its detailed model within monolayer MoS₂ in Fig. 2e).

Geometric phase analysis (GPA) was also performed on the ADF-STEM image to draw the strain fields of these SMACs in Fig. 2f (see Methods section). The MoS₂ lattice parameter was selected as the reference. An apparent compressive strain around

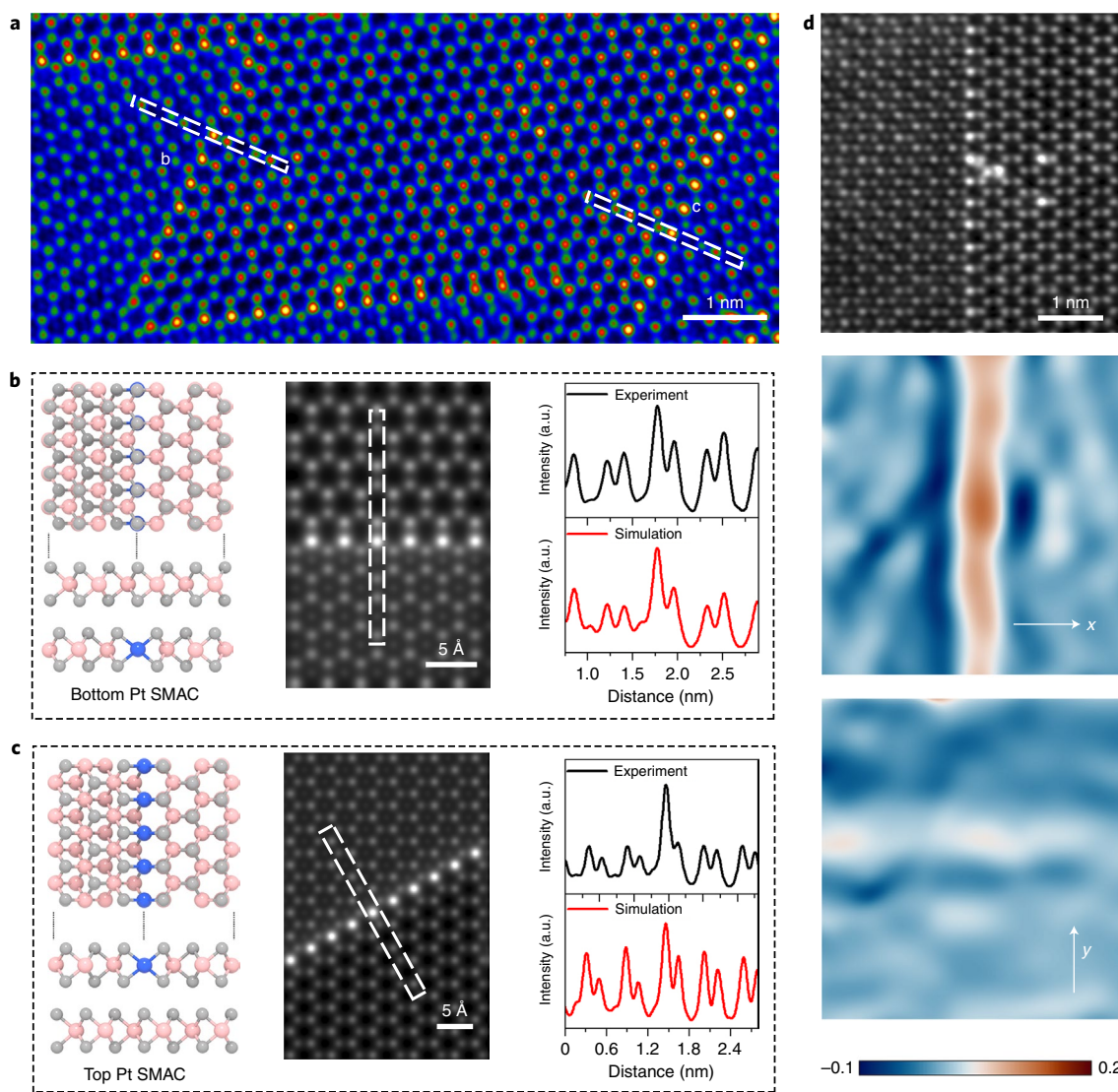


Fig. 3 | Atomic structure of platinum SMACs in bilayer MoS₂. **a**, False-coloured ADF-STEM image of a bilayer MoS₂ region. **b**, Atomic structure of platinum SMACs in the bottom layer of MoS₂, as shown with the structural schematic (left), simulated STEM image (middle) and intensity profiles (right) along the white dashed box in **a**, as well as the corresponding simulated STEM image. **c**, Atomic structure of platinum SMACs in the top layer of MoS₂, as shown with structural schematic (left), simulated STEM image (middle) and intensity profiles (right) along the white dashed box in **a**, as well as the corresponding simulated STEM image. **d**, Top panel: magnified ADF-STEM image of a platinum SMAC in bilayer MoS₂, including ϵ_{xx} strain (middle) and ϵ_{yy} strain (bottom). Atom colours are the same as in Fig. 2e.

the two sides of the platinum SMAC is observed along the x -axis (ϵ_{xx} , the direction perpendicular to SMAC), but negligible along the y -axis (ϵ_{yy} , the direction parallel to SMAC). We note that the ϵ_{xx} compressive strain is as high as $5.5 \pm 1.1\%$, indicating an effective uniaxial SMAC-localized in-plane strain.

To study the possible interlayer influence between platinum SMACs and MoS₂ layer, we examined the structure of the SMAC in bilayer MoS₂. On applying the false-colour treatment on STEM images, the typical 3R and 2H stacking registries become distinguishable through the weak atom blobs in each honeycomb. As shown in Fig. 3a, platinum SMACs are mainly present at a lateral 3R|2H|3R hybrid structure in bilayer MoS₂, which has a stacking sequence of AB|AA|BA (ref. 26). Intriguingly, we found two types of platinum SMAC structures in bilayer MoS₂: Pt atoms in the bottom (Fig. 3b) and top (Fig. 3c) layers. The latter usually shows a brighter contrast than that of the former in the STEM imaging. The corresponding intensity profiles can be used to distinguish them (see right panels in Fig. 3b,c). We also applied GPA to probe the strain

distribution around platinum SMACs in bilayer MoS₂ (Fig. 3d), which exhibits a phenomenon similar to that of monolayer MoS₂ (Fig. 2f), with a stronger compressive strain along the x -axis than that along the y -axis. Note that in bilayer MoS₂ the formed strain around the platinum SMAC is considerably averaged in both the bottom and top layers, thus exhibiting a weaker strain phase profile than that of the monolayer counterpart.

Formation mechanism. To elucidate the formation mechanism of platinum SMACs, we carried out the density functional theory (DFT) calculations (see Methods for details). First, by comparing the formation energy of a set of Pt-MoS₂ systems, we searched for the energy-optimal geometry for platinum atoms attached to the MoS₂ lattice. Among the enumerated structures, a four-coordinated motif (Pt-S₄)—in which the single platinum atom covalently bonds with four sulfur atoms at the edge of MoS₂—gives the lowest binding energy (Supplementary Fig. 13). Such a structure is also confirmed by our high-resolution characterization of the MoS₂ edge

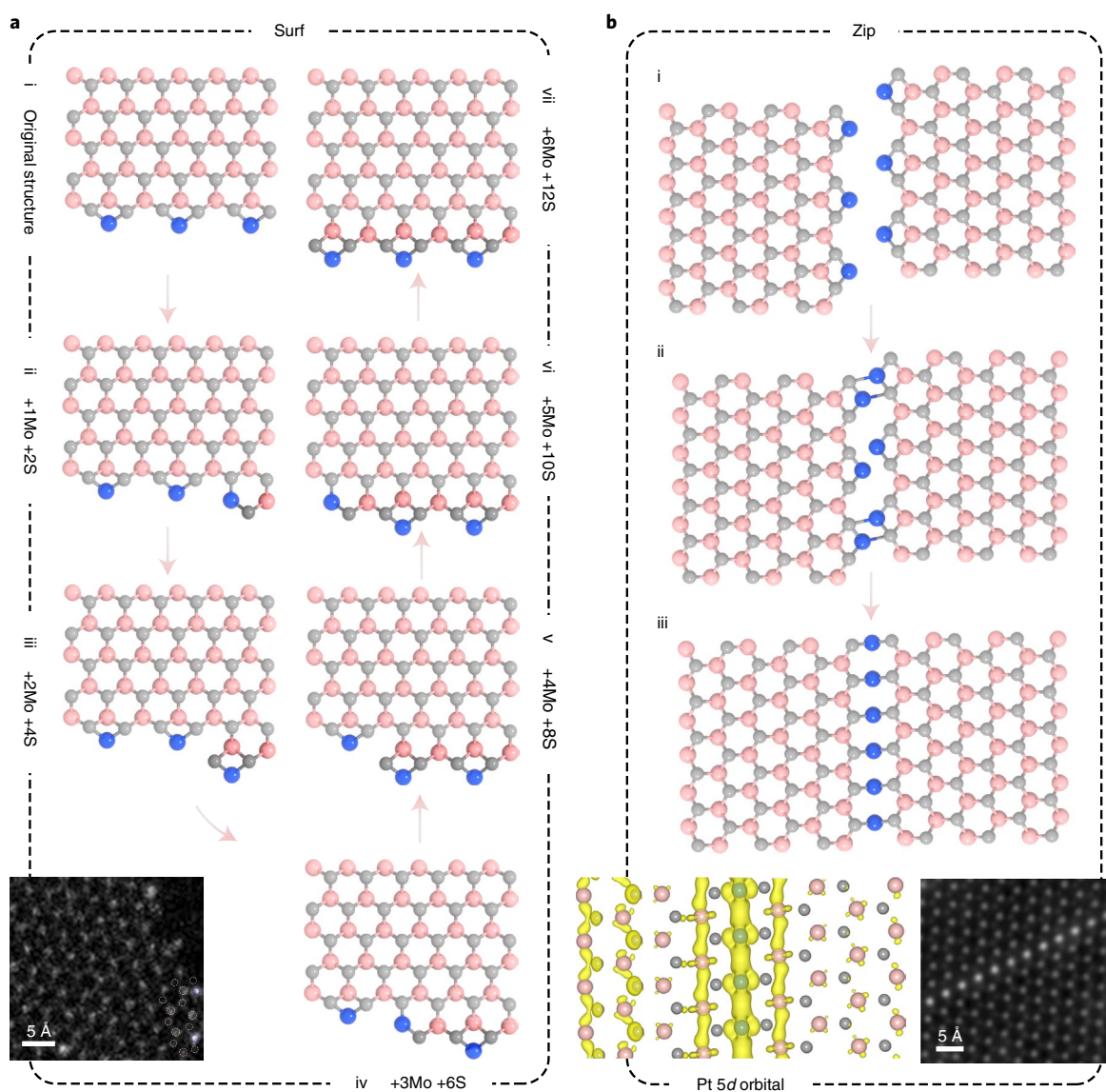


Fig. 4 | Formation mechanism of platinum SMACs. **a**, Energetically optimal atomic configurations i–vii during the step-by-step addition of MoS₂ units to a platinum-passivated zigzag edge. The feeding species for each step are Mo + 2S. The growth leads to kink movement, shifting platinum atoms as though they surf along the growth front by the coming feeding species. The bottom STEM image presents the evidence of the lowest-energy intermediate state (iv). **b**, The formation of platinum SMACs. Platinum atoms along two zigzag edges zip together (ii, iii) when two inversely oriented platinum-terminated MoS₂ domains meet each other. The STEM image corresponds to the formation of a complete platinum SMAC. The insets are isosurface plots (0.033776 e Å⁻³) of the partial charge density distribution of platinum 5d orbitals. A substantial overlap of electron densities between adjacent platinum atoms can be well-identified. Atom colours are the same as in Fig. 2e.

(Fig. 4a, bottom). Following the chemisorption of more platinum atoms, we note that the energetically most favourable configuration is an ordered array of adjacent Pt-S₄ motifs along the MoS₂ edge (Supplementary Fig. 14). Second, we explored possible dynamical evolution of the adsorbed platinum atoms during the growth of a MoS₂ domain. In our calculations, MoS₂ units were added step-by-step to the platinum-terminated zigzag edge. At each step, various platinum attached sites were examined to ensure the optimal configuration (see configurational spectra at each growth step in Supplementary Fig. 16). These results indicate that the configurations that perfectly extend the MoS₂ lattice are in low-energy regions. The evolution of atomic configurations along the lowest-energy pathway is presented in Fig. 4a, manifesting the flow of kinks along the platinum-passivated edge. Briefly, the Pt-S₄ motif first evolves into a new kink hexagon (Fig. 4a_{iii}) and later into a

MoS₂ hexagon (Fig. 4a_{iii}), which is also experimentally evidenced at a domain edge (Fig. 4a, bottom). Later, the continuous feeding of molybdenum and sulfur atoms moves the kink to complete the growth of a new row, resulting in one-MoS₂ lattice-constant migration of the platinum-terminated edge along the growth direction (Fig. 4a_{vii}). We thus call this dynamical evolution the surfing of platinum atoms, that is, the Pt-S₄ motifs will migrate to the growth front during the growing process.

Based on the above calculations, platinum atoms could zip them together by keeping the Pt-S₄ motifs, when two inversely oriented domains with similar Pt-termination connect laterally. This process yields a chain of platinum atoms covalently embedded in the MTB, namely, platinum SMAC (Fig. 4b). *Ab initio* molecular dynamics simulations suggest that the chain has excellent structural stability and can sustain an elevated temperature as high as 1,000 K

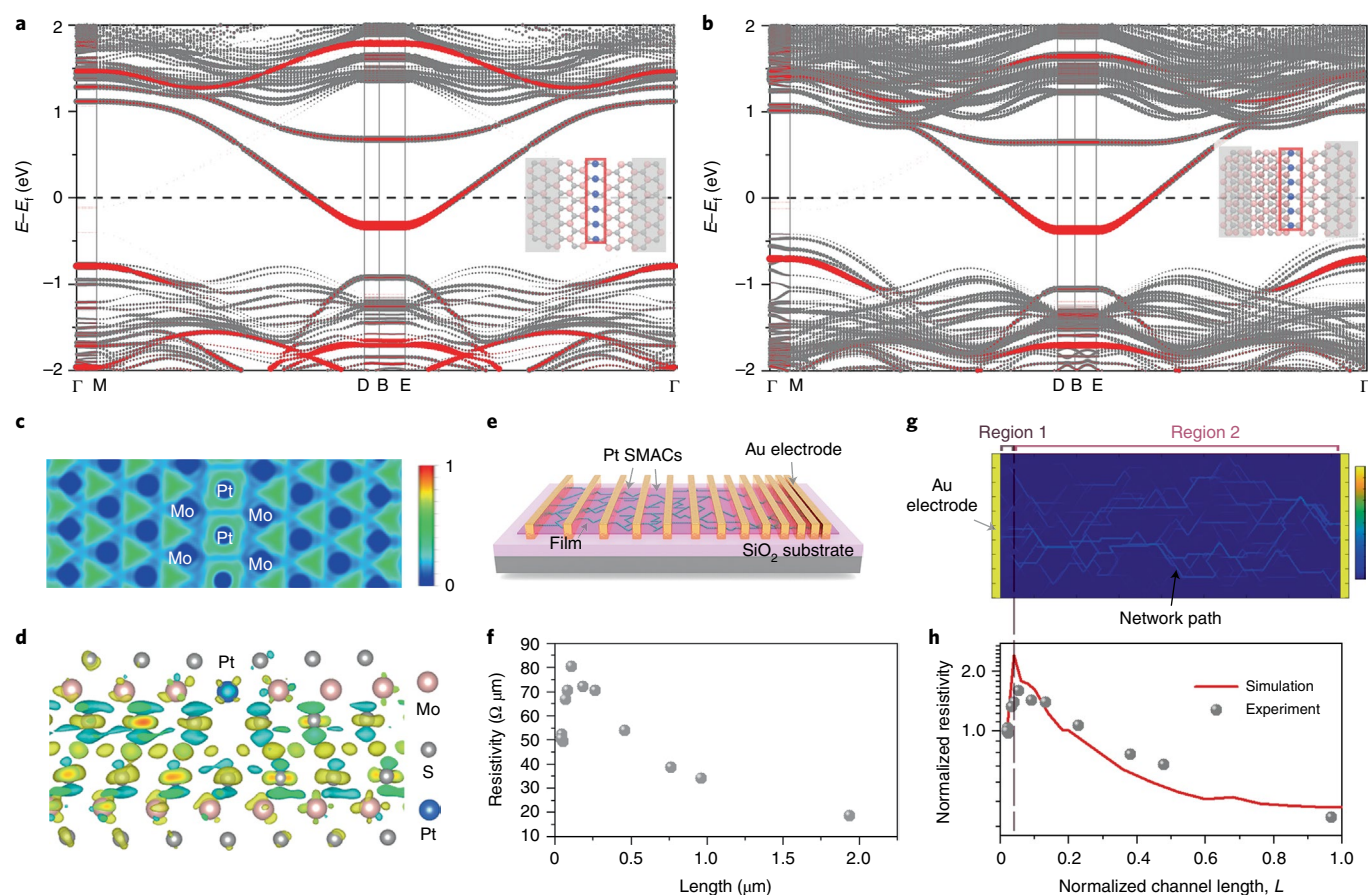


Fig. 5 | Electronic structure of platinum SMAC. **a,b**, Electronic band structures of a platinum SMAC embedded in monolayer **(a)** and bilayer **(b)** MoS₂. The band structures are projected onto just the platinum atoms as well as those atoms in the bulk area (unshaded regions in the atomic structure). The weight character of bands is thickness encoded. Red lines mark the contribution of the platinum plus the sulfur atoms directly bonded to them. The grey lines represent the whole platinum SMACs/MoS₂ system. **c**, Electron localization function map of platinum SMACs in a monolayer MoS₂ on the (001) plane. There is only weak electronic localization between adjacent platinum atoms. **d**, Isosurface plot (0.00016 e Å⁻³) of charge density difference between a SMAC-containing MoS₂ layer and a pristine MoS₂ layer (side view). The charge accumulation and depletion regions are distinguished by yellow and blue, respectively. **e**, Schematic illustration of transmission-line model devices. The device structures with channel lengths from 2 μm to 50 nm are fabricated, and the channel width is defined to be 1 μm. **f**, Room temperature resistivity as a function of channel length extracted using a typical two-terminal transmission-line model device. **g**, Current colour map calculated for the device with the largest channel length of *L* (normalized value of 1, corresponding to 2 μm in the experiment). **h**, Normalized simulated resistivity and experimental results versus channel length.

(Supplementary Fig. 19). We also studied the energy-optimized structure of platinum SMACs in bilayer MoS₂ using *ab initio* molecular dynamics simulations, showing that the platinum SMACs are favorably formed at the grain boundaries between 2H and 3R phased MoS₂ bilayers (Supplementary Fig. 15), in good agreement with the atomic structure shown in Fig. 3b,c.

Metallic behaviour of platinum SMACs. The highly ordered platinum SMACs possess a larger interatomic distance than platinum metal (3.2 Å versus 2.78 Å), determined by the host MoS₂ MTB. To examine the possible interaction in platinum SMACs, we further investigate the partial charge density distribution of platinum 5*d* orbitals (the inset of Fig. 4b). Apart from localized bonding electrons between sulfur and platinum atoms, we also note substantial delocalized electron densities between adjacent platinum atoms, rendering SMACs as electronic transport channels. We then calculated the band structure and projected density of states of the SMACs, confirming the metallic behaviour (see Supplementary Fig. 20 and the red data points in Fig. 5a,b); this is in sharp contrast to the case of scattered platinum atoms. This metallic behaviour is attributed to the substantial overlap of platinum electronic states,

stemming from the Pt–Pt spacing of less than 0.9 nm in our platinum SMACs. On the contrary, platinum atoms with a neighbour distance exceeding 1.5 nm (for example, single scattered platinum atoms) possess a highly localized defect band level, hindering the electronic transport (Supplementary Fig. 17). Electron localization function (ELF) further supports this result from the covalent interaction between platinum and sulfur atoms (Supplementary Fig. 21) as well as electronic delocalization between platinum atoms along the chain (Fig. 5c). Moreover, charge transfer analysis between two stacked MoS₂ layers indicates that platinum atoms in the top MoS₂ layer donate electrons to sulfur atoms in the bottom MoS₂ layer (Fig. 5d), which is in good accordance with the two types of Pt(II) signals in the XPS spectra (Fig. 1c).

To verify this metallic behaviour of platinum SMACs, we fabricated a series of FET devices with channel lengths ranging from 2 μm down to 50 nm; the channel width was kept constant at 1 μm (Fig. 5e and Supplementary Fig. 22). It is observed that the resistivity of the sample is around two orders of magnitude lower than that of CVD-grown MoS₂ (Fig. 5f and Supplementary Fig. 24)^{27,28}. Moreover, the resistivity exhibits an initial linear increase and later a critical transition from high to low value, demonstrating a volcano-like

relationship with the channel length (l). To further elaborate on this phenomenon, we adopt the complex network-based method (a powerful tool for simulating carrier transport in nanostructured film^{29–31}) to investigate the electronic transport behaviour of platinum SMACs within MoS₂ film. The trend of the calculated resistivity shows a length dependence that is consistent with the experimental results (Fig. 5h). Furthermore, the visualization of the current distribution confirms that carrier conduction proceeds by percolation through the platinum atomic chains for all length scales (Fig. 5g). Specifically, at shorter channel lengths (region 1), the termination of percolative pathways³² causes an increased resistivity. At longer channel lengths (region 2), the high density of Y-shaped platinum SMACs junctions—which are formed due to the merging of MoS₂ grains—considerably enhances the conductivity of the channel (see Supplementary Note 2 for detailed discussion). Expectedly, our one-dimensional metallic chains can provide a model system to study interacting electrons, such as Tomonaga–Luttinger liquid and charge density waves^{33–36}.

Conclusion

In summary, we developed a facile and effective chemical vapour co-deposition strategy to fabricate a wafer-scale network of platinum SMACs with remarkable stability. The atomic structures and electronic properties of platinum SMACs were extensively studied in monolayer and bilayer MoS₂ films. Combining DFT analysis with experimental results, we proposed a surf-zip growth mechanism to reveal the growth process of platinum SMACs, and later successfully extended to grow cobalt SMACs via our co-deposition method (Supplementary Fig. 18). Moreover, we found a metallic behaviour of platinum SMACs originated from the substantial overlap of platinum electronic states, which can facilitate the electronic conduction of atom-thin films via percolation through SMAC networks. Finally, our work offers a promising route to fabricate air-stable SMACs on a large-scale, and provides one of the smallest one-dimensional platforms for studying Luttinger liquids, the Fermi-liquid microscopic model, and other theoretical one-dimensional models.

Methods

Synthesis of wafer-scale platinum SMACs inside MoS₂ films. First, the platinum films were deposited on clean SiO₂/Si or sapphire wafers using electron-beam evaporation with a speed of 0.1 Å s⁻¹ for 10 s. Second, the as-prepared platinum-coated SiO₂/Si wafers were used as the substrates for the CVD of MoS₂ films (Supplementary Fig. 3). To be more precise, the substrates were placed facing down on an aluminium oxide boat containing MoO₃ powders in the middle of a quartz tube reaction chamber, and sulfur powders were loaded in another crucible upstream in the tube. Third, after purging the CVD system by 500 standard cubic centimetres per minute (sccm) argon flow for 3 min, the centre of the furnace was heated from room temperature to growth temperature with a ramp of ~50 °C min⁻¹ under continuous argon gas of 60 sccm. The platinum SMACs inside MoS₂ films were synthesized by keeping the temperature of molybdenum sources at 650 °C for 4 min, whereas sulfur sources at around 230 °C. Finally, the furnace was naturally cooled down under the protective argon atmosphere.

Material characterization. Raman spectra were collected on a Renishaw inVia microscope under 532 nm laser at room temperature. The spot size is about 1 μm in diameter. The chemical states of obtained samples were analysed by X-ray photoelectron spectroscopy (Kratos AXIS Supra XPS with a monochromatic Al Kα source). Peak positions were all corrected by the carbon 1s spectrum at 284.8 eV.

ADF-STEM imaging and analysis. The as-prepared samples on the SiO₂/Si or sapphire wafers were transferred to the TEM grid for the STEM characterizations with the mediator of polymethyl methacrylate. To avoid the hydrocarbon contamination during electron microscopy studies, all of the TEM samples were baked at 200 °C for 8 h under vacuum before the microscopy experiment; furthermore, ADF-STEM imaging and EDS mapping were conducted using an aberration-corrected FEI ChemiSTEM operated at 200 kV with an approximately 20 pA probe current. The high signal-to-noise ratio ADF-STEM images are obtained by an image series composed of thirty fast exposure images of the same region followed by a post-acquisition image distortion correction and averaging, in which each pixel time was fixed at less than 6 μs to avoid substantial beam damage. The ADF-STEM signal was collected at an angle range of 46–200 mrad with an

electron-beam convergence angle of 24.7 mrad. The occupied sites by platinum atoms were confirmed by comparing the experimental ADF-STEM images and simulated results. The simulation of the ADF-STEM images was performed with the Dr. Probe package³⁷, and the simulated parameters were fixed based on the experimental conditions. The strain analysis was performed with the GPA method using a dedicated script for the DigitalMicrograph software³⁸, in which the strain was calculated with the reference of a perfect MoS₂ lattice.

Device fabrication. Electron-beam lithography was used to define a rectangular channel region (2 μm × 150 μm) of platinum SMAC/MoS₂ film on SiO₂/Si substrate. The rest platinum SMAC/MoS₂ film was etched away by CHF₃ plasma at -20 °C for 40 s. Ti/Au (5 nm/20 nm) electrodes were defined by the electron-beam lithography process followed by the electron-beam evaporation and lift-off process.

Electrical characterization. An Agilent B1500A semiconductor device parameter analyser was used to examine the transport properties at room temperature in a vacuum chamber of 10⁻² Torr. Standard direct current sweeps are carried out to evaluate the transfer characteristics of all devices.

Ab initio molecular dynamics simulations for platinum SMACs in monolayer MoS₂

In this model, the edges are passivated with sulfur atoms. The related calculations were mainly implemented in the Vienna Ab initio Simulation Package^{39–41}, using spin-polarized DFT based on the generalized gradient approximation of the Perdew–Burke–Ernzerhof functional⁴². The core region was described by a projector augmented-wave method with a plane-wave kinetic energy cutoff of 500 eV. The vacuum region was set to 15 Å to isolate neighbouring periodic images. The Brillouin zone was sampled with a (1 × 20 × 1) k -point mesh for geometry optimizations, whereas a (1 × 30 × 1) mesh was used for electronic structure calculations. The self-consistency convergence criteria for the total energies were set to 10⁻⁶ eV, and all atomic positions and cell shapes were optimized using the Gaussian smearing method until the force component on each atom is below 0.01 eV Å⁻¹. The valences of molybdenum, sulfur and platinum were set to 6, 6 and 10, respectively. After structural optimization, the platinum atoms reside in the mirror twin boundary coordinated by four adjacent sulfur atoms. The interatomic distance in the chain is 3.19 Å. This is very close to the experimental value (3.15 Å). For electronic structure calculation, we performed an electronic self-consistent field procedure with tetrahedron method using Blöchl corrections. The thermal stability of platinum SMAC in MoS₂ structure was evaluated by an ab initio molecular dynamic simulation using NVT ensemble. The simulation was run at 1,000 K, and the time step was set to 1 fs over 30 ps.

Formation mechanism calculations. The binding energy of a single platinum atom on monolayer MoS₂. To investigate the energy preferred configuration of a single platinum atom on monolayer MoS₂, we calculated the binding energy of platinum atom at different sites of MoS₂. The calculation formula of binding energy is

$$E_b = E_{\text{MoS}_2 + \text{Pt}} - E_{\text{MoS}_2} - E_{\text{Pt}}$$

where $E_{\text{MoS}_2 + \text{Pt}}$ is the total energy of the system when platinum is adsorbed on MoS₂, E_{MoS_2} is the energy of MoS₂ and E_{Pt} is the energy of a single platinum atom.

Initial structure justification (DFT-optimized stable Pt-S₄ configuration).

To determine the most stable arrangement of platinum atoms on the MoS₂ edge, we selected four representative structures and calculated their average binding energy of Pt-S. The average binding energy is defined as

$$E_{b-\text{aver}} = (E_{\text{MoS}_2 + n\text{Pt}} - E_{\text{MoS}_2} - nE_{\text{Pt}})/n$$

Among them, $E_{\text{MoS}_2 + n\text{Pt}}$ is the total energy of the system, E_{MoS_2} is the energy of MoS₂, E_{Pt} is the energy of a single platinum atom and n is the number of platinum atoms.

Electronic properties calculations. *ELF.* The electron localization function (ELF)^{43,44} was used to examine the localized characteristics of electrons. Its value is between 0 and 1. The upper limit value of 1 means that the electron is completely localized, whereas 0 means that the electron is completely delocalized. In the calculated the local charge density shown in Fig. 5c, blue represents 0 and red represents 1. It can be found that there is no bond between adjacent platinum atoms, and an electron distribution similar to a covalent bond is formed between sulfur and platinum.

Charge density difference calculation. Charge density difference map is generally plotted to view the redistribution of charges after the interaction. Through the calculation and analysis of differential charge density, it is possible to obtain the properties of charge redistribution and the direction of bonding polarization in the process of bonding and electronic coupling. The definition formula of differential charge density is:

$$\Delta\rho = \rho_{\text{bilayer MoS}_2} - \rho_{\text{MoS}_2 - \text{Pt layer}} - \rho_{\text{MoS}_2 \text{ layer}}$$

where $\rho_{\text{bilayer MoS}_2}$ is the charge density of the entire system, $\rho_{\text{MoS}_2-\text{Pt layer}}$ is the charge density of the MoS₂-Pt layer, and $\rho_{\text{MoS}_2 \text{ layer}}$ is the charge density of the perfect MoS₂ layer. Figure 5d indicates that charge transfer happens between the platinum atom in the first MoS₂ layer and the sulfur atoms in the second MoS₂ layer.

Complex network-based method. A representative platinum SMAC inner MoS₂ film of dimension $L \times \frac{L}{2}$ is occupied by a uniformly generated random distribution of platinum SMACs and line defects, and the background MoS₂, as shown in Supplementary Fig. 25b. Widthless platinum SMACs were randomly dispersed in the simulation film with an area density of about 9.4%. We used randomly generated coordinates ($x_{\text{Pt}}, y_{\text{Pt}}$) as the centre of a platinum SMAC (note that $0 < x_{\text{Pt}} < L, 0 < y_{\text{Pt}} < \frac{L}{2}$). Based on our STEM images, we imposed threefold symmetry with random overlap for platinum SMACs. Similarly, the line defects were randomly dispersed in the film with an area density of about 10.3%. Random coordinates ($x_{\text{defect}}, y_{\text{defect}}$) established the centre of the defects and random angle θ with respect to the horizontal direction for its orientation. The generated platinum SMACs inner MoS₂ film was then converted into a complex network graph by a universal discretization approach²⁹. We assumed line defects as insulators with infinite resistance, background MoS₂ as resistors with resistance 1,000 times larger than platinum SMACs. Then we converted the model into a resistor network and implemented the network by MATLAB. By solving Kirchhoff's current law and Ohm's law, we calculated the overall resistance and the distribution of current.

Data availability

All data are available in the main text or Supplementary Information.

Code availability

The code of the complex network-based method employed in this work is available at <https://doi.org/10.6084/m9.figshare.c.4879863>.

Received: 20 April 2021; Accepted: 28 January 2022;

Published online: 14 March 2022

References

- Li, H. et al. Synergetic interaction between neighbouring platinum monomers in CO₂ hydrogenation. *Nat. Nanotechnol.* **13**, 411–417 (2018).
- Ahn, J., Yeom, H., Yoon, H. & Lyo, I.-W. Metal-insulator transition in Au atomic chains on Si with two proximal bands. *Phys. Rev. Lett.* **91**, 196403 (2003).
- Gambardella, P. et al. Ferromagnetism in one-dimensional monatomic metal chains. *Nature* **416**, 301–304 (2002).
- Pham, T. et al. Torsional instability in the single-chain limit of a transition metal trichalcogenide. *Science* **361**, 263–266 (2018).
- Dua, P., Lee, G. & Kim, K. S. Ferromagnetism in monatomic chains: spin-dependent bandwidth narrowing/broadening. *J. Phys. Chem. C* **121**, 20994–21000 (2017).
- Bergman, A., Hellsvik, J., Bessrab, P. F. & Delin, A. Spin relaxation signature of colossal magnetic anisotropy in platinum atomic chains. *Sci. Rep.* **6**, 36872 (2016).
- Rubio-Bollinger, G., Bahn, S. R., Agrait, N., Jacobsen, K. W. & Vieira, S. Mechanical properties and formation mechanisms of a wire of single gold atoms. *Phys. Rev. Lett.* **87**, 026101 (2001).
- Ohnishi, H., Kondo, Y. & Takayanagi, K. Quantized conductance through individual rows of suspended gold atoms. *Nature* **395**, 780–783 (1998).
- Kizuka, T. Atomic configuration and mechanical and electrical properties of stable gold wires of single-atom width. *Phys. Rev. B* **77**, 155401 (2008).
- Sokolov, A., Zhang, C., Tsybmal, E. Y., Redepenning, J. & Doudin, B. Quantized magnetoresistance in atomic-size contacts. *Nat. Nanotechnol.* **2**, 171–175 (2007).
- Autès, G., Barreateau, C., Desjonquères, M. C., Spanjaard, D. & Viret, M. Giant orbital moments are responsible for the anisotropic magnetoresistance of atomic contacts. *Europhys. Lett.* **83**, 17010 (2008).
- Calvo, M. R. et al. The Kondo effect in ferromagnetic atomic contacts. *Nature* **458**, 1150–1153 (2009).
- Oncel, N. Atomic chains on surfaces. *J. Phys. Condens. Matter* **20**, 393001 (2008).
- Snijders, P. C. & Weitering, H. H. Colloquium: electronic instabilities in self-assembled atom wires. *Rev. Mod. Phys.* **82**, 307–329 (2010).
- Blumenstein, C. et al. Atomically controlled quantum chains hosting a Tomonaga–Luttinger liquid. *Nat. Phys.* **7**, 776–780 (2011).
- Yanson, A. et al. Formation and manipulation of a metallic wire of single gold atoms. *Nature* **395**, 783–785 (1998).
- Lehtinen, O. et al. Atomic scale microstructure and properties of Se-deficient two-dimensional MoSe₂. *ACS Nano* **9**, 3274–3283 (2015).
- Ma, Y. et al. Angle resolved photoemission spectroscopy reveals spin charge separation in metallic MoSe₂ grain boundary. *Nat. Commun.* **8**, 14231 (2017).
- Zhou, W. et al. Intrinsic structural defects in monolayer molybdenum disulfide. *Nano Lett.* **13**, 2615–2622 (2013).
- Ma, Y. et al. Metallic twin grain boundaries embedded in MoSe₂ monolayers grown by molecular beam epitaxy. *ACS Nano* **11**, 5130–5139 (2017).
- Nanda, K. K., Sahu, S. N. & Behera, S. N. Liquid-drop model for the size-dependent melting of low-dimensional systems. *Phys. Rev. A* **66**, 013208 (2002).
- Voiry, D. et al. The role of electronic coupling between substrate and 2D MoS₂ nanosheets in electrocatalytic production of hydrogen. *Nat. Mater.* **15**, 1003–1009 (2016).
- Vancsó, P. et al. The intrinsic defect structure of exfoliated MoS₂ single layers revealed by scanning tunneling microscopy. *Sci. Rep.* **6**, 29726 (2016).
- Fu, Y., Rudnev, A. V., Wiberg, G. K. & Arenz, M. Single graphene layer on Pt(111) creates confined electrochemical environment via selective ion transport. *Angew. Chem. Int. Ed.* **56**, 12883–12887 (2017).
- Xu, S. et al. Direct integration of strained-Pt catalysts into proton-exchange-membrane fuel cells with atomic layer deposition. *Adv. Mater.* **33**, 2007885 (2021).
- Xia, M. et al. Spectroscopic signatures of AA' and AB stacking of chemical vapor deposited bilayer MoS₂. *ACS Nano* **9**, 12246–12254 (2015).
- Liu, H. et al. Switching mechanism in single-layer molybdenum disulfide transistors: an insight into current flow across Schottky barriers. *ACS Nano* **8**, 1031–1038 (2014).
- Jin, G. et al. Atomically thin three-dimensional membranes of van der Waals semiconductors by wafer-scale growth. *Sci. Adv.* **5**, eaaw3180 (2019).
- Yao, H., Hsieh, Y.-P., Kong, J. & Hofmann, M. Modelling electrical conduction in nanostructure assemblies through complex networks. *Nat. Mater.* **19**, 745–751 (2020).
- Albert, R. & Barabási, A.-L. Statistical mechanics of complex networks. *Rev. Mod. Phys.* **74**, 47–97 (2002).
- Lee, D., Kahng, B., Cho, Y. S., Goh, K. I. & Lee, D. S. Recent advances of percolation theory in complex networks. *J. Korean Phys. Soc.* **73**, 152–164 (2018).
- Yao, H., Hempel, M., Hsieh, Y.-P., Kong, J. & Hofmann, M. Characterizing percolative materials by straining. *Nanoscale* **11**, 1074–1079 (2019).
- Jolie, W. et al. Tomonaga–Luttinger liquid in a box: electrons confined within MoS₂ mirror-twin boundaries. *Phys. Rev. X* **9**, 011055 (2019).
- Barja, S. et al. Charge density wave order in 1D mirror twin boundaries of single-layer MoSe₂. *Nat. Phys.* **12**, 751–756 (2016).
- Nagao, T., Yaginuma, S., Inaoka, T. & Sakurai, T. One-dimensional plasmon in an atomic-scale metal wire. *Phys. Rev. Lett.* **97**, 116802 (2006).
- Segovia, P., Purdie, D., Hengsberger, M. & Baer, Y. Observation of spin and charge collective modes in one-dimensional metallic chains. *Nature* **402**, 504–507 (1999).
- Barthel, J. Dr. Probe: a software for high-resolution STEM image simulation. *Ultramicroscopy* **193**, 1–11 (2018).
- Hÿtch, M. et al. Nanoscale holographic interferometry for strain measurements in electronic devices. *Nature* **453**, 1086–1089 (2008).
- Kresse, G. & Hafner, J. Ab initio molecular dynamics for liquid metals. *Phys. Rev. B* **47**, 558 (1993).
- Kresse, G. & Furthmüller, J. Efficiency of ab-initio total energy calculations for metals and semiconductors using a plane-wave basis set. *Comput. Mater. Sci.* **6**, 15–50 (1996).
- Kresse, G. & Hafner, J. Ab initio molecular-dynamics simulation of the liquid-metal–amorphous-semiconductor transition in germanium. *Phys. Rev. B* **49**, 14251–14269 (1994).
- Perdew, J. P., Burke, K. & Ernzerhof, M. Generalized gradient approximation made simple. *Phys. Rev. Lett.* **77**, 3865 (1996).
- Silvi, B. & Savin, A. Classification of chemical bonds based on topological analysis of electron localization functions. *Nature* **371**, 683–686 (1994).
- Savin, A., Nesper, R., Wengert, S. & Fässler, T. F. ELF: the electron localization function. *Angew. Chem. Int. Ed.* **36**, 1808–1832 (1997).

Acknowledgements

This work was supported by the support from National Research Foundation Singapore programme NRF-CRP22-2019-0007 and NRF-CRP21-2018-0007. This work is also supported by the Ministry of Education, Singapore, under its AcRF Tier 2 (MOE2019-T2-2-105) and AcRF Tier 1 RG4/17 and RG7/18. This research is also supported by A*STAR under its AME IRG Grant (project no. A2083c0052). The work at NUA was supported by the National Key Research and Development Program of China (2019YFA0705400), National Natural Science Foundation of China (11772153, 22073048), the Natural Science Foundation of Jiangsu Province (BK20190018), and a Project by the Priority Academic Program Development of Jiangsu Higher Education Institutions. W.Z. acknowledges the support of the Beijing Outstanding Young Scientist Program (BJJWZYJH01201914430039). B.T. and X.W. acknowledge the support from the Ministry of Education, Singapore (MOE2019 T1-001-113). H.Y. and M.N. acknowledge the support from the Hong Kong Research Grant Council, Hong Kong (HKRGC GRF 12300218, 12300519, 17201020, 17300021, and UGC-RMGs 207300829).

H.D. acknowledges the support from German Research Foundation (DFG) under the Grant SFB917 Nanoswitches.

Author contributions

Z.L., Y.H. and Z.Z. guided the project. S.G. and Y.H. synthesized the platinum SMACs. S.G. conducted electronic measurements. J.F. and C.Z. (NTU and SEU) conducted the STEM characterizations. Z.Z. proposed the surf-zip model. P.Z. and Z.Z. performed the first-principle calculations and analysed the simulation results. H.Y., M.H., Y.H. and M.N. simulated the electronic transport. Z.L., Y.H., Z.Z. and C.J. conceived and supervised the experiments. All the authors discussed the results and commented on the manuscript.

Competing interests

The authors declare no competing interests.

Additional information

Supplementary information The online version contains supplementary material available at <https://doi.org/10.1038/s44160-022-00038-z>.

Correspondence and requests for materials should be addressed to Chunlin Jia, Zhuhua Zhang, Yongmin He or Zheng Liu.

Peer review information *Nature Synthesis* thanks Jan van Ruitenbeek and the other, anonymous, reviewer(s) for their contribution to the peer review of this work. Alison Stoddart was the primary editor on this article and managed its editorial process and peer review in collaboration with the rest of the editorial team.

Reprints and permissions information is available at www.nature.com/reprints.

Publisher's note Springer Nature remains neutral with regard to jurisdictional claims in published maps and institutional affiliations.

© The Author(s), under exclusive licence to Springer Nature Limited 2022